

Shape-related optical and catalytic properties of wurtzite-type CoO nanoplates and nanorods

This content has been downloaded from IOPscience. Please scroll down to see the full text.

2014 Nanotechnology 25 035707

(<http://iopscience.iop.org/0957-4484/25/3/035707>)

View [the table of contents for this issue](#), or go to the [journal homepage](#) for more

Download details:

IP Address: 59.77.43.191

This content was downloaded on 12/07/2015 at 08:36

Please note that [terms and conditions apply](#).

Shape-related optical and catalytic properties of wurtzite-type CoO nanoplates and nanorods

Aolin Lu, Yuanzhi Chen, Deqian Zeng, Meng Li, Qingshui Xie, Xiangxin Zhang and Dong-Liang Peng

Department of Materials Science and Engineering, College of Materials, Xiamen University, Xiamen 361005, People's Republic of China

E-mail: yuanzhi@xmu.edu.cn and dlpeng@xmu.edu.cn

Received 1 August 2013, revised 24 November 2013


Accepted for publication 28 November 2013

Published 20 December 2013

Abstract

In this paper, we report the anisotropic optical and catalytic properties of wurtzite-type hexagonal CoO (h-CoO) nanocrystals, an unusual nanosized indirect semiconductor material. h-CoO nanoplates and nanorods with a divided morphology have been synthesized via facile solution methods. The employment of flash-heating and surfactant tri-*n*-octylphosphine favors the formation of plate-like morphology, whereas the utilization of cobalt stearate as a precursor is critical for the synthesis of nanorods. Structural analyses indicate that the basal plane of the nanoplates is (001) face and the growth direction of the nanorods is along the *c* axis. Moreover, the UV–vis absorption spectra, the corresponding energy gap and the catalytic properties are found to vary with the crystal shape and the dimensions of the as-prepared h-CoO nanocrystals. Furthermore, remarkable catalytic activities for H₂ generation from the hydrolysis of alkaline NaBH₄ solutions have been observed for the as-prepared h-CoO nanocrystals. The calculated Arrhenius activation energies show a decreasing trend with increasing extension degree along the ⟨001⟩ direction, which is in agreement with the variation of the charge-transfer energy gap. Finally the maximum hydrogen generation rate of the h-CoO nanoplates exceeds most of the reported values of transition metal or noble metal containing catalysts performing in the same reaction system, which makes them a low-cost alternative to commonly used noble metal catalysts in H₂ generation from the hydrolysis of borohydrides, and might find potential applications in the field of green energy.

Keywords: wurtzite CoO, solution synthesis, nanocrystals, catalyst, hydrogen generation

 Online supplementary data available from stacks.iop.org/Nano/25/035707/mmedia

(Some figures may appear in colour only in the online journal)

1. Introduction

Transition metal oxides have received great attention due to their various properties and wide applications. In particular, cobalt oxides are potentially useful in many fields such as solar collectors [1], lithium-ion battery materials [2, 3], catalysts [4–6], gas sensors [7, 8], data memory devices [9, 10] and so on. One of the important cobalt oxides is cobalt monoxide (CoO). CoO typically has two crystalline phases:

rock-salt CoO (c-CoO, space group *Fm3m*) with octahedral Co²⁺, and wurtzite-type hexagonal CoO (h-CoO, space group *P63mc*) with tetrahedral Co²⁺ [11]. The crystal structure of wurtzite-type CoO which was first reported by Redman and Steward [12] is nearly the same as wurtzite-type hexagonal ZnO, and this phase has been regarded as metastable in the bulk and able to stabilize in mixed cobalt oxides (Zn_{1-x}Co_xO) [13] or ultrathin epitaxial films [14]. Recently, Nam *et al* found that the formation of h-CoO was kinetically

controlled in conditions of rapid heating at high temperature while that of c-CoO was thermodynamically controlled through prolonged heating at low temperatures [3].

For c-CoO nanocrystals, many synthetic routes have been reported. However, there are fewer reported methods for the synthesis of h-CoO, probably due to its extraordinary nature which sets strict conditions for preparation. For example, pencil-shaped h-CoO was synthesized by the thermal decomposition of a cobalt–oleate complex [15]. Moreover, Seo *et al* [11] reported the synthesis of h-CoO nanorods and nanopyramids by thermal deposition of $\text{Co}(\text{acac})_3$ simultaneously in oleylamine, and found that a prolonged reaction time of 3 h would yield stable phase c-CoO, in response to the report of Nam who demonstrated that in the complex of $\text{Co}(\text{acac})_3$ and benzylamine, adding 1,2-dichlorobenzene in the solution before the deposition reaction would yield h-CoO rods instead of pyramids, and more 1,2-dichlorobenzene added would lead to the formation of c-CoO cubes [3]. In general, the reported synthetic methods for h-CoO nanocrystals are relatively complicated and time-consuming, and the shapes of synthesized nanocrystals restricted to pyramids or rods.

Up to now, a large portion of the research about the properties of h-CoO focused on the magnetic properties [3, 11, 15–17] and the phase transition properties. For example, h-CoO may transfer into c-CoO in the pressure range of 0.8–6.9 GPa [18] or above a temperature of 378 °C [19]. Recently, h-CoO has been found to exhibit characteristic electrochemical properties toward lithium [3]. Cu-doped h-CoO shows high initial Coulombic efficiency and ultrahigh capacity with excellent cycling performance as an anode material [20]. In contrast, explorations of the optical and catalytic properties of h-CoO nanocrystals are not common.

It has been affirmed that, for bulk single crystal, morphology plays an important role in the intrinsic chemical and physical properties [21–23]. Several studies also have focused on the influence of nanocrystal morphology on properties. For example, the catalytic selectivity of Pt nanocrystal was found to be strongly affected by the shape [24]. TiO_2 nanosheets exposing a high percentage of (001) facets show excellent photocatalytic efficiency [25]. In addition, considering wurtzite-type ZnO nanocrystals, the connection between morphology and properties is important [26]. However, systematic studies regarding this connection of h-CoO nanocrystals have not been reported.

In this study, we report the solution synthesis of h-CoO nanoplates with mainly exposed (001) facets and nanorods with a divided morphology. The relationship between the shape and optical and catalytic properties was investigated. Interestingly, the exposed crystalline facet and the dimensions of the as-prepared nanocrystals influence their energy gaps of charge-transfer and d–d transition. Finally, remarkably high catalytic activities for H_2 generation from the hydrolysis of alkaline NaBH_4 solutions have been found for the as-prepared h-CoO nanocrystals. In particular, the catalytic activity of h-CoO nanoplates is found to be superior to that of many noble metal catalysts, which makes them an excellent

candidate to be applied in H_2 generation from the hydrolysis of various borohydrides, and might find potential applications in the field of green energy.

2. Experimental section

2.1. Synthesis

2.1.1. Synthesis of h-CoO hexagonal nanoplates. In a typical experiment, 0.3 mmol of cobalt (II) acetylacetonate ($\text{Co}(\text{acac})_2$, 98%, Acros) and 10 ml of oleylamine (OAm, 80–90%, Acros) were placed into a flask and then the mixed solution was heated to 353 K under vigorous stirring and kept at this temperature for 30 min. After the solution was cooled down to 323 K, 1 mmol of tri-*n*-octylphosphine (TOP, 97%, Strem) was injected into the solution, and the temperature was maintained at 323 K for 10 min. Then, the reaction was initiated by flash-heating the solution to 493 K. After the solution was kept at 493 K for 60 min, it was cooled down to room temperature. The whole process was conducted under a flow of high-purity argon gas. 10 ml of acetone was then added to the blue–green suspension and centrifugation was employed to separate the product. The obtained precipitate was then washed with hexane three times and dried in air.

2.1.2. Synthesis of h-CoO nanorods. In a typical experiment, 0.3 mmol of cobalt (II) stearate ($\text{Co}(\text{st})_2$, 95%, Acros) and 10 ml of 1-octadecene (ODE, 90%, Acros) were placed into a flask and then the mixed solution was heated to 403 K under vigorous stirring and kept at this temperature for 60 min to remove water. Then, the solution was flash heated to 585 K for 60 min to obtain short nanorods or to 591 K for 60 min to obtain long nanorods before it was cooled down to room temperature. The whole process was conducted under a flow of high-purity argon gas. 10 ml of ethanol was then added to the blue–green suspension and centrifugation was employed to separate the product. The obtained precipitate was then washed with hexane five times and dried in air.

2.2. Structural characterization

For the transmission electron microscopy (TEM) analyses, a portion of the as-prepared powders was dispersed in toluene via ultrasound concussion for 15 min. Then the particle suspensions in toluene were dropped onto a Cu grid coated with carbon film before drying at room temperature under ambient conditions. TEM images and selective area electron diffraction (SAED) data were collected on a JEM-2100 transmission electron microscope operating at 200 kV.

The samples for x-ray diffraction (XRD) analyses were prepared by dropping the powder suspensions in toluene onto a glass wafer before drying at room temperature under ambient conditions. XRD measurements were taken on a Panalytical X'pert PRO diffractometer using $\text{Cu K}\alpha$ radiation, operating at 40 kV and 30 mA.

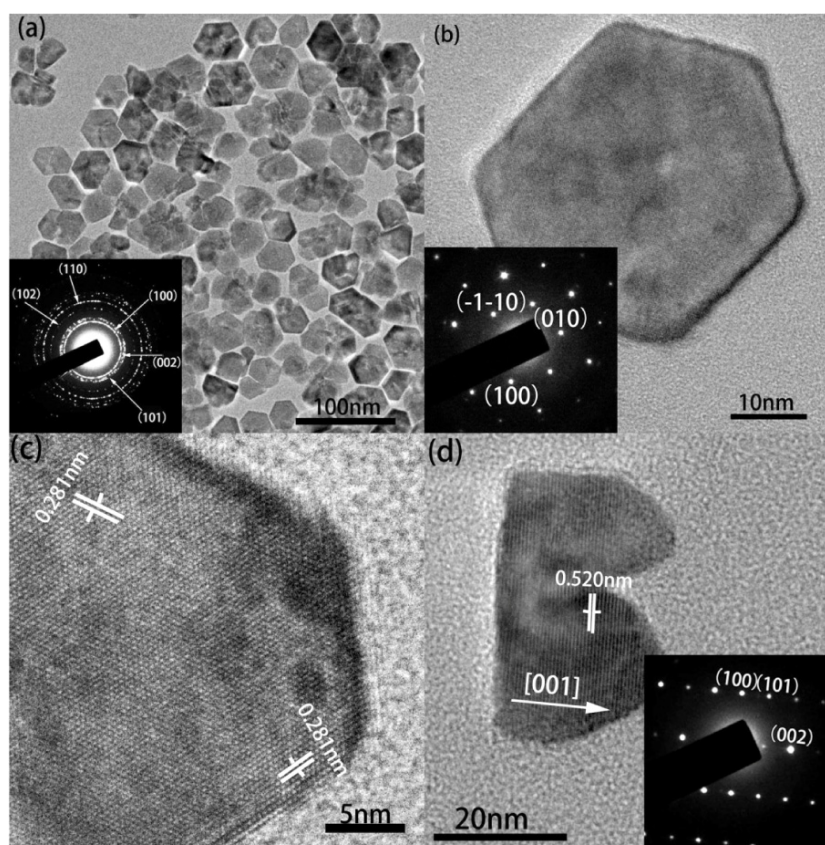


Figure 1. (a) Low-magnification TEM image of as-prepared h-CoO nanoplates with corresponding SAED pattern (inset). (b), (c) TEM and HRTEM images respectively of a typical hexagonal nanoplate. The SAED pattern (inset in (b)) is viewed in the [001] direction of h-CoO. (d) HRTEM image showing the side view of a single nanoplate along with the SAED pattern (inset) viewed in the [010] direction.

2.3. Property characterization

X-ray photoelectron spectroscopy (XPS) analyses were performed using a PHI Quantum 2000 scanning ESCA Microprobe spectrometer using an Al $K\alpha$ photon source. UV-vis spectra were obtained at room temperature with a Shimadzu UV-2550 ultraviolet-visible spectrophotometer.

For the testing of catalytic properties, 6 ml of alkaline NaBH_4 solution containing 10 wt% NaBH_4 and 10 wt% NaOH was injected into a rubber plug sealed flask which contained 10 mg of as-prepared h-CoO catalysts. The volume of hydrogen generated from the hydrolysis reaction of NaBH_4 solution in the presence of h-CoO catalysts was measured using the water-displacement method. The reaction temperature was controlled by immersing the flask in a temperature-controlled water bath which was equipped with a magnetic stirring apparatus. Hydrolysis experiments were also conducted at various temperatures ranging from 283 to 323 K.

3. Results and discussion

3.1. Synthesis and morphology of the h-CoO nanoplates

Figure 1(a) shows the low-magnification TEM image of the as-prepared h-CoO nanoplates which typically have an

average edge length of 50 nm and a thickness of about 20 nm. The SAED pattern (figure 1(a) inset) recorded from randomly distributed nanocrystals exhibits diffraction rings that correspond to wurtzite-type hexagonal CoO. In addition, it is noticeable that the intensity of the (002) diffraction ring is relatively much weaker than that of the (100), (101) and (110) rings, which actually suggests confined extension along the c axis during the growth of the plate-shaped h-CoO. Figure 1(b) shows the TEM image of a single nanoplate with a hexagon shape. The corresponding SAED pattern reveals single crystalline characteristics and can be indexed in the [001] zone axis of hexagonal structure. The HRTEM image (figure 1(c)) also reveals a highly crystalline structure with a lattice spacing of 0.281 nm which corresponds to the (100) plane of h-CoO. Additionally, as shown in figure S1 (available at stacks.iop.org/Nano/25/035707/mmedia), some nanoplates may have a non-standard hexagonal shape with three long edges and three neighboring short edges, which reflects the difference between (100) and (010) planes. Furthermore, a small number of nanocrystals appear as a rectangle with two or three humps on one long edge. They actually correspond to the side view of the nanoplates. The corresponding HRTEM image and SAED pattern are shown in figure 1(d), which demonstrates the basal (001) plane with a d -spacing of 0.520 nm. Obviously, the SAED pattern reveals single crystalline characteristics and a growth direction of [001] in

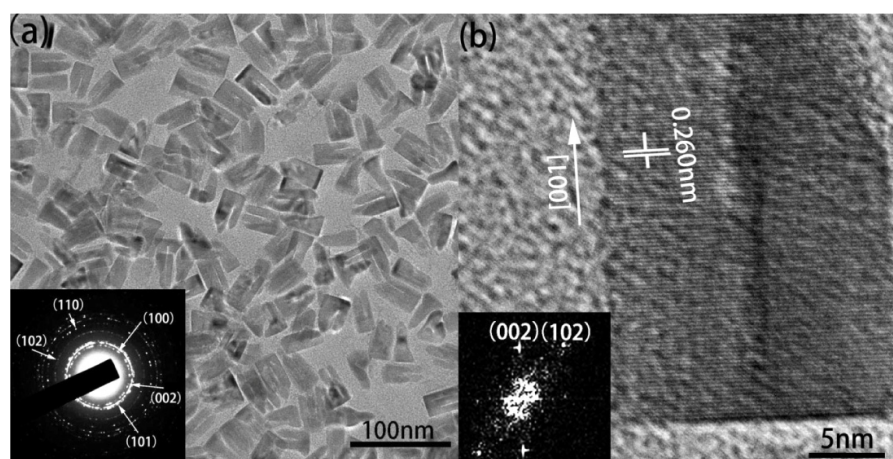


Figure 2. (a) Low-magnification TEM image of h-CoO short nanorods along with the corresponding SAED patterns (inset). (b) HRTEM image of a single short nanorod along with the FFT pattern (inset) in the [010] zone axis.

the plate thickness. Such morphology with humps indicates that the growth of the nanoplate along the c axis is not a uniform process. The EDS spectrum (figure S2 available at stacks.iop.org/Nano/25/035707/mmedia) recorded from a single nanoplate shows the presence of Co and O elements, confirming the oxide nature.

In general, thermal decomposition of cobalt acetylacetonate–amine complex yields hexagonal pyramids [3, 11, 16, 19], and the nucleation of h-CoO would happen in the solution below 473 K [3, 11, 19]. However, according to our research, the presence of TOP in the solution will raise the nucleation temperature of h-CoO so that it will not result in the fcc-CoO impurity which tends to occur at a lower reaction temperature. Hence, 1 mmol TOP was added and the reaction temperature was kept at 493 K. Previously, TOP was regarded as a critical surfactant in the synthesis of monodispersed transition metal nanoparticles [27], Ni–Au core–shell nanoparticles [28], and 1D metal phosphine nanostructures [29, 30]. Recently, we found that TOP could play an important role in the synthesis of octahedral fcc-CoO nanocrystals [5]. In this study, the function of TOP is a little similar to that of 1,2-dichlorobenzene discovered by Nam *et al* [3]. The effect of TOP may be due to the steric hindrance of the three carbon chains in its molecule, which possibly changes the kinetic control condition to the thermodynamic control condition. On the other hand, the hindrance of TOP may make the crystals grow in a more orderly manner when the decomposition of the precursor is rapid in this kinetic control condition, so that the plate-like morphology of the nanocrystals can be maintained.

3.2. Synthesis and morphology of the h-CoO nanorods

Figure 2(a) is the typical TEM image of the as-prepared h-CoO short nanorods with an average width of about 20 nm and a length of about 50 nm (20 nm \times 50 nm) synthesized at 585 K. Most nanorods split into two or three pencil-shaped subrods, which may be due to the relatively high growth rate along the rods. The SAED pattern (figure 2(a) inset) reveals

a wurtzite-type hexagonal structure. However, the intensity of the (002) ring is more distinct, and that of the (100) and the (101) rings is relatively gloomy, implying preferential growth along [001] direction. The single crystalline nature is further confirmed by HRTEM image (figure 2(b)) which shows that the well-defined lattice fringes go straight through the whole structure without stacking faults. The lattice spacing of 0.260 nm can be assigned to the (002) plane of wurtzite structure. The corresponding fast Fourier transform (FFT) pattern (figure 2(b) inset) of the HRTEM image also verifies that this single crystalline nanorod grows along the [001] direction.

In the syntheses, we found that if the reaction temperature rose, the aspect ratio of the nanorods would increase. This may be due to the faster growth rate along the rods at a high temperature. The TEM image (figure 3(a)) of the products synthesized at 591 K shows a slim long-rod morphology with an average width of about 5 nm and a length of about 70 nm (5 nm \times 70 nm). Many of the nanorods also split into two or more subrods. The recorded SAED pattern (figure 3(a) inset) can be indexed to a wurtzite-type hexagonal structure and the (002) diffraction ring exhibits a bright contrast because of strongly preferred orientation. The HRTEM image in figure 3(b) exhibits visible lattice fringes assigned to the (001) plane with a lattice spacing of 0.520 nm. The identified growth direction is also [001].

The XRD patterns (figure S3 available at stacks.iop.org/Nano/25/035707/mmedia) of the as-prepared h-CoO nanoplates, short nanorods (20 nm \times 50 nm) and long nanorods (5 nm \times 70 nm) show diffraction peaks corresponding well to the wurtzite-type hexagonal structure, although the signals are weak because of the absorption of Cu $K\alpha$ radiation by Co.

3.3. Discussion on the formation mechanism

The above results indicate that the reaction conditions play an important role in the formation of the final morphology of h-CoO nanocrystals. In the formation processes of hexagonal

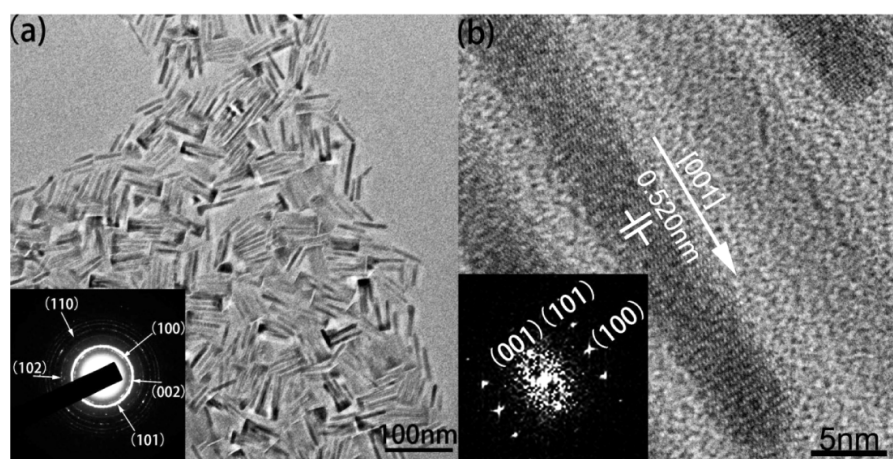
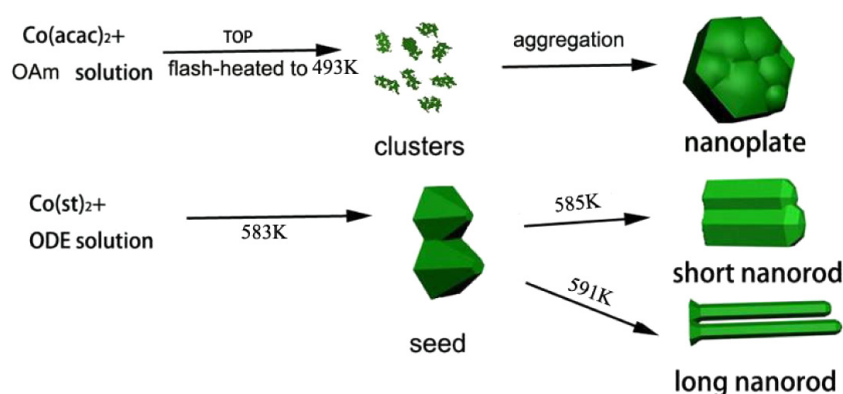


Figure 3. (a) Low-magnification TEM image of h-CoO long nanorods along with the corresponding SAED pattern (inset). (b) HRTEM image of a single long nanorod along with the FFT pattern (inset) in the [010] zone axis.



Scheme 1. Schematic illustration of the formation of h-CoO nanoplates and nanorods.

plates (scheme 1), the decomposition of $\text{Co}(\text{acac})_2$ takes place rapidly to generate h-CoO clusters (figure S4(a) available at stacks.iop.org/Nano/25/035707/mmedia) with a high concentration since the solution is flash heated to reaction temperature, and the solution color instantly changes from transparent orange to blue. Then, h-CoO nanoclusters tend to aggregate along the face parallel to the (001) planes, which is confirmed from the corresponding SAED pattern (figure S4(b) available at stacks.iop.org/Nano/25/035707/mmedia) in which it shows that the (002) diffraction ring is rather weak compared to the (100), (101) and (110) diffraction rings. The aggregated nanoclusters further develop into plate-like morphology and the growth along the [001] direction is restrained in the forming process. Due to the unstable polar (001) plane consisting of Co^{2+} ions, humps can be formed on one side of the nanoplate so as to reduce the exposed area of the (001) plane.

For the formation of rod-shaped h-CoO nanocrystals, $\text{Co}(\text{st})_2$ was used as a precursor, since it decomposes at a relatively low speed, which makes the aspect ratio controllable by temperature and reaction time. The solution remains transparent at the reaction temperature for about 20 min and then the solution color gradually changes to non-transparent blue, indicating the formation of seeds.

By increasing the aging time, the formed seeds would grow longer and become $20 \text{ nm} \times 40 \text{ nm}$ pyramid nanocrystals (figure S5 available at stacks.iop.org/Nano/25/035707/mmedia). Divided morphology can be observed in many of these nanocrystals. An *et al* reported the synthesis of pencil-shaped h-CoO nanorods with a similar morphology by the thermal decomposition of Co-oleate complex in ODE, and the aspect ratio of rods was influenced by the heating rate and aging time [15]. Finally the formed pyramid nanocrystals will develop into nanorods by further increasing the aging time. The formation mechanism of rod-shape h-CoO can be similar to that of ZnO rods [31]. The relatively unstable polar (001) plane exposed by metal ions (see figure 4) grows fast and becomes a pencil point; however, the basal oxygen (00 $\bar{1}$) plane on the bottom of the rod and the nonpolar low-index {100} planes are relatively stable and become the main exposed faces.

3.4. XPS spectra

The surface condition has important influences on the catalytic properties. To verify the surface chemical states of the as-prepared h-CoO nanocrystals, XPS spectra were recorded. Figure 5 shows the XPS spectra of Co 2p and O 1s

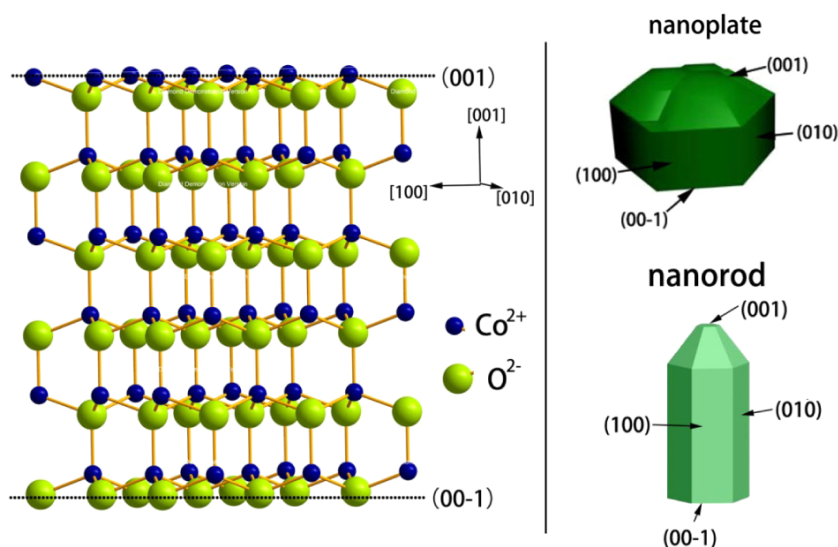


Figure 4. Left: crystal structure of wurtzite-type h-CoO. The (001) plane is exposed with Co^{2+} ions and the (00 $\bar{1}$) plane is exposed with O^{2-} ions. Right: corresponding crystalline models for h-CoO nanoplates and nanorods.

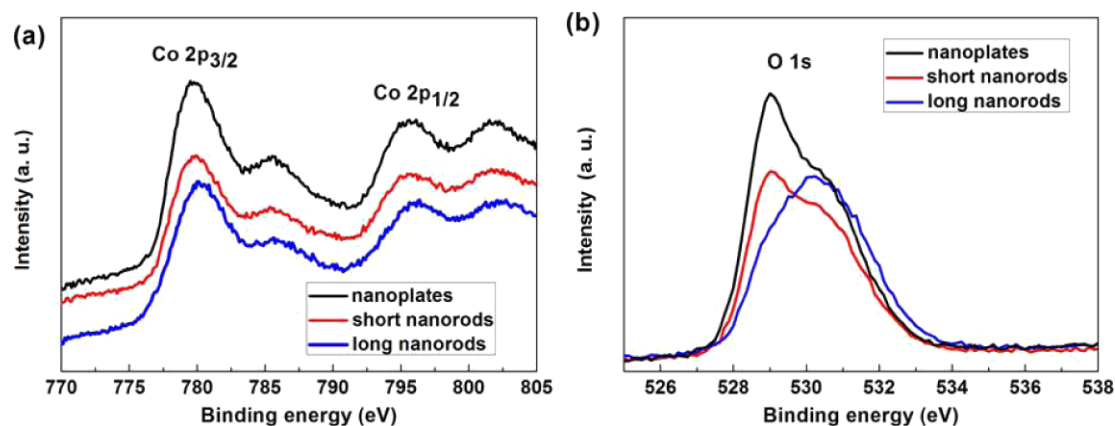


Figure 5. XPS spectra of the Co 2p (a) and O 1s (b) regions for the h-CoO nanoplates, short nanorods and long nanorods.

regions of the three kinds of h-CoO nanocrystals. The peaks at 780.1 and 795.9 eV are attributed to Co (II) $2p_{3/2}$ and Co (II) $2p_{1/2}$ energy levels, respectively, which is in agreement with the reported values of fcc-CoO [32]. There were no significant differences among the three spectra, indicating that the octahedral-coordinated O^{2-} ions of fcc-CoO and the tetrahedral-coordinated O^{2-} ions of h-CoO make no difference on the Co 2p spectra.

The typical shake-up lines at 786 and 802 eV confirm the chemical form of CoO [33] rather than Co_3O_4 [34], and no features appear at 778.1 eV, revealing that no elemental Co exists. The O 1s spectra can be decomposed into two peaks (see figure S6 available at stacks.iop.org/Nano/25/035707/mmedia): the peak at 529.1 eV (O_L) can be due to lattice oxygen in the Co–O bond of h-CoO. Additionally, similar to fcc-CoO [35] and ZnO [26], the second peak at a higher energy of 530.4 eV (O_C) can be due to the chemisorbed and dissociated oxygen species. For the long nanorods, the O_C peak is stronger than the O_L peak compared with the other two h-CoO crystals, which might be due to the characteristics of long nanorods: smallest grain size, high specific surface area

and the mainly exposed {100} faces composed of equivalent O^{2-} and Co^{2+} ions. For the nanoplates with the smallest specific surface area, though the (001) face only is exposed with Co^{2+} ions, growth of the humps can reduce the exposure of the (001) face and the amount of exposed Co^{2+} ions, thus leading to the reduced O_C peak.

3.5. Electronic absorption and energy gap.

The anisotropy of the h-CoO lattice indicates that its properties would highly depend on the shapes and dimensions of the nanocrystals [17]. Figure 6(a) shows the normalized room-temperature UV–vis absorption spectra of the three as-prepared h-CoO samples. Three conjoint absorption peaks at 587, 631, and 674 nm, which are respectively associated with $4A_2 \rightarrow 2E(G)$, $4A_2 \rightarrow 2A_1(G)$ and $4A_2 \rightarrow 4T_1(P)$ d–d crystal field transitions in the high spin state of Co^{2+} in tetrahedral coordination [13, 36, 37], are observed in the visible region. The positions of the three d–d transition peaks hardly vary with the grain morphology. However, it

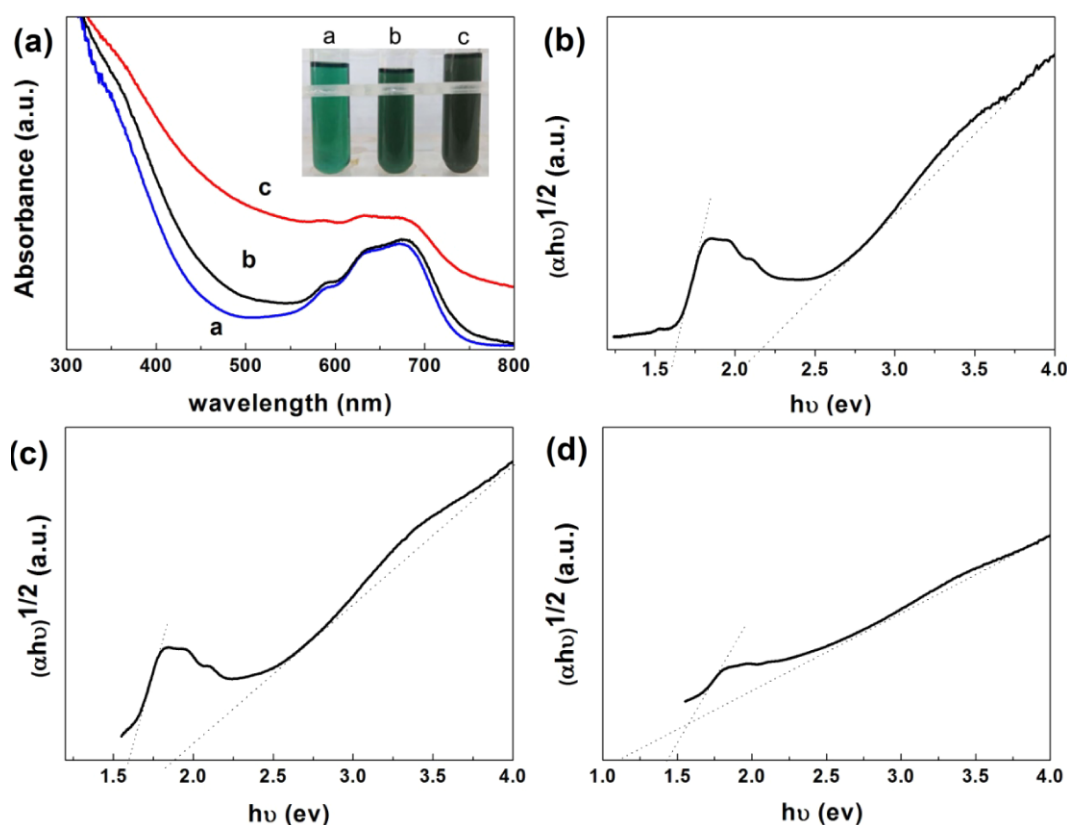


Figure 6. (a) UV-vis absorption spectra and the corresponding photographs of toluene-dispersed h-CoO nanoplates (curve a), short nanorods (curve b) and long nanorods (curve c); (b), (c) and (d) are the optical bandgap energies of nanoplates, short nanorods and long nanorods, respectively.

is noticeable that the nanoplates and the short nanorods demonstrate relatively strong d-d transition peaks and the long nanorods gain a weaker one, which reveals that the d-d transitions might enhance as the h-CoO crystals have a confined dimension along the $\langle 001 \rangle$ direction. Additionally, the background absorption of the short nanorods is a little higher than that of the nanoplates, while that of the long nanorods shows the highest background absorption. This demonstrates that the visible-light transmittance would decrease with increasing $\langle 001 \rangle$ oriented degree. The colors (figure 6(a) inset) of the three toluene-dispersed h-CoO solutions also vary with crystalline morphologies: for the nanoplates, it is blue-green; for the short nanorods, it becomes green; for the long nanorods, it is dark green. This result is in accordance with the UV-vis absorption spectra which reveal that the absorption coefficient at blue light (near 495 nm) increases with the $\langle 001 \rangle$ oriented degree of the h-CoO nanocrystals. Moreover, no individual d-d transition peaks (figure S7 available at stacks.iop.org/Nano/25/035707/mmedia) can be observed in fcc-CoO nanocrystals synthesized using the method mentioned in a previous study [5], which may be for the reason that, according to crystal field theory, crystal field splitting energy is greatly affected by the coordination mode of surrounding ions. The Co^{2+} d-d energy level in octahedral sites of fcc-CoO is very different from that in O tetrahedron sites of hcp CoO [36, 38].

Similar to ZnO, the strong absorption edges at the high-energy region ($\lambda < 500$ nm) are due to the charge-transfer

(CT) transitions [13, 39]. However, unlike ZnO which is a direct bandgap semiconductor, the energy gap of h-CoO was calculated to be 1.5 eV with an indirect gap from the local spin density approximation + U level of theory [40], and an indirect energy gap of 2.3 eV at 5 K was observed by magnetic circular dichroism spectra [13]. The bandgap E_g can be acquired from the electron absorption spectra using the equation as follows:

$$(\alpha h\nu)^n = B(h\nu - E_g) \quad (1)$$

where α is the absorption coefficient, $h\nu$ is the photon energy, B is a constant value relative to the characteristics of the material, and n equals 1/2 for an indirect transition, or 2 for a direct transition.

The plots of $(\alpha h\nu)^{1/2}$ versus $h\nu$ of the three h-CoO samples are shown in figures 6(b)–(d), which show that the optical energy gap of h-CoO is also strongly influenced by the morphology. Each curve can be linearly fitted into two lines with the intercepts at two energy gaps: E_{g1} which derives from the spectra < 500 nm represents the CT transfer gap, and the other one E_{g2} which comes from the d-d transitions can be representative of the d-d energy gap. The values of E_{g1} for the nanoplates, short nanorods and long nanorods are 2.16, 1.88 and 1.13 eV, respectively. The values of E_{g2} for the three h-CoO samples are 1.62, 1.60 and 1.43 eV, respectively, illustrating that the CT energy gap decreases drastically with the increase of the $\langle 001 \rangle$ oriented degree while the d-d transition energy gap decreases a little. It is

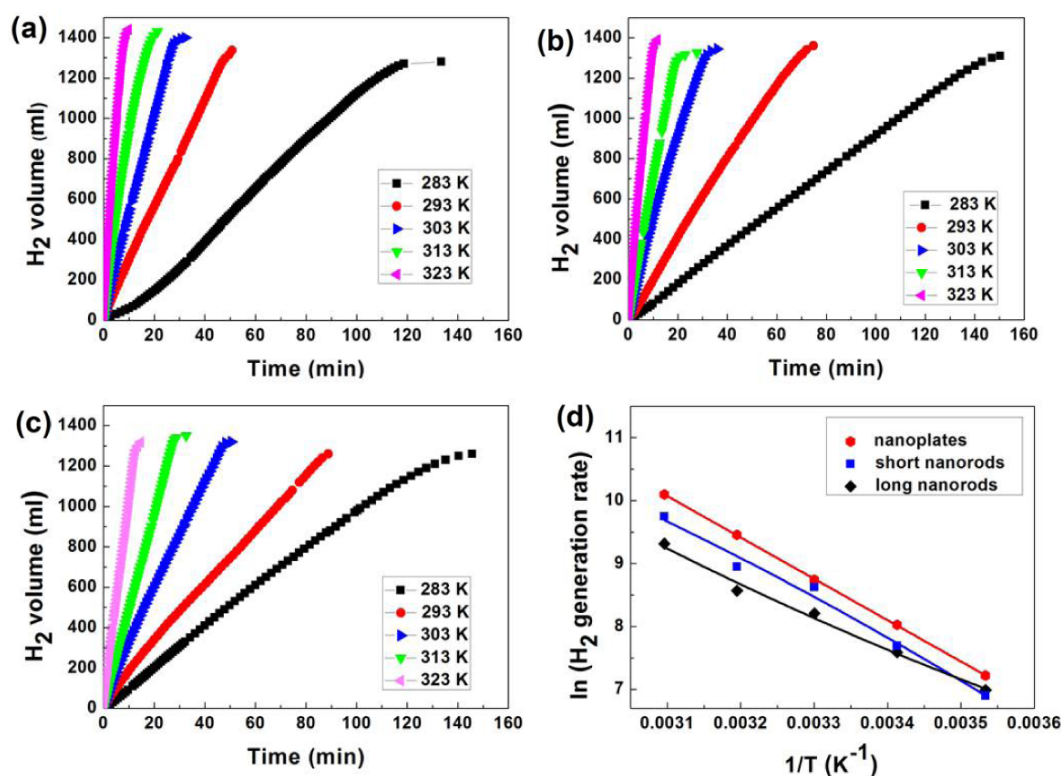


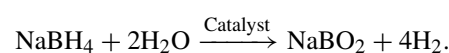
Figure 7. The hydrogen generation rates for h-CoO nanoplates (a), short nanorods (b) and long nanorods (c) at different temperatures in solutions containing 10 wt% NaOH, 10 wt% NaBH₄ and 10 mg catalyst. (d) The corresponding Arrhenius plots ($\ln r$ versus $1/T$) obtained from data shown in (a), (b) and (c).

remarkable that for a nanoscale indirect semiconductor, the crystalline preferential orientation plays an important role in the energy gap. For a nanoscale direct semiconductor, such as CdSe [41], the bandgap and fluorescence properties vary with the grain shape and surface properties, which respectively account for the different dimension quantum confinements and surface energy states that may trap charge carriers at the surface. For an indirect semiconductor such as Si, the quantum confinement was believed to make a nanoscale Si direct semiconductor, which was confirmed by PL research toward a Si nanostructure [42, 43]. For h-CoO nanocrystals, probably due to the relatively loose atomic configuration along the (001) direction according to the nature of h-CoO, the constraint on CT is weaker than directions perpendicular to (001), that is to say quantum confinements might be weaker along the (001) direction when the lengths of every direction are the same. Hence, the long nanorod demonstrates the lowest energy gap though it only has one degree of freedom and gains the smallest volume among the three h-CoO samples. The fact that the CT energy gap can be tunable by alerting the extension degree along the (001) direction while the (001) extension has little influence on the d-d transition energy gap may be because the d-d transition occurs in one Co²⁺ ion, and for the same crystal lattice, this transition is less influenced by the crystalline orientation.

3.6. Catalytic properties

Chemical hydrides are considered as a convenient hydrogen source with high densities of hydrogen available. However,

suitable catalysts are usually needed to control the release of hydrogen. One of the important catalytic applications for CoO nanomaterials is that they can be used as active catalysts for the generation of hydrogen from the hydrolysis of alkaline NaBH₄ solutions [5]. The equation of hydrogen generation reaction upon NaBH₄ hydrolysis at ambient temperature in the presence of suitable catalysts is as follows [44]:



To the best of our knowledge, the catalytic properties in the above reaction of h-CoO nanomaterials have not been reported. It is therefore interesting to check the catalytic properties of h-CoO nanocrystal catalysts. The plots of H₂ generation volume as a function of time of three as-prepared h-CoO nanocrystal samples tested at five temperatures are demonstrated in figures 7(a)–(c). As expected, the H₂ generation rate increases with temperature. However, the catalytic properties are different, depending strongly on their shapes. For each testing temperature, the time needed from the start of the hydrolysis reaction to the end by using the nanoplates is the shortest while that by using the long nanorods is the longest, except for the case at 283 K. Table S1 (available at stacks.iop.org/Nano/25/035707/mmedia) summarizes the maximum H₂ generation rates which are acquired from the initial stage of each run by using the three catalysts. It is noticeable that for the nanoplates, the maximum H₂ generation rate is as high as 6250 ml min⁻¹ g⁻¹ at 303 K. This value exceeds most of the reported values of

transition metal catalysts or noble metal containing catalysts performed in the same condition. Compared to the nanoplates, the short nanorods and long nanorods exhibit less superior catalytic activities, and the obtained maximum H₂ generation rates are 5555 and 3665 ml min⁻¹ g⁻¹ at 303 K, respectively. The observed different catalytic activities of the three h-CoO samples may also be due to their different preferential orientations as well as exposed facets. For nanoplates, the (001) plane which is exposed with O anion at the flat underside is the mainly exposed surface and it is not electrically neutral. Thus, for the NaBH₄ hydrolysis reaction, which is a redox reaction, a polar surface would promote it more than a neutral surface. For the nanorods, the area of polar surface is decreasing as the rod becomes longer. Consequently, the catalytic activity would decrease.

The Arrhenius activation energy (E_a) for the catalytic reaction can be calculated using the following equation:

$$r = k_0 \exp\left(-\frac{E_a}{RT}\right) \quad (2)$$

where r represents the reaction rate, k_0 is the reaction constant, R is the universal gas constant and T is the reaction temperature. From the Arrhenius plots (figure 7(d)), the E_a values of nanoplates, short nanorods and long nanorods are calculated to be about 55.3, 53.0 and 42.7 kJ mol⁻¹, respectively. The decreasing trend of Arrhenius activation energies with increasing extension degree along the (001) direction is also in agreement with the variation of the CT energy gap, which illustrates that the trigger of catalytic reaction might be relevant to the charge transition of different ions in the catalyst lattice, so the long nanorods with the lowest CT energy gap exhibit the smallest E_a value compared with that of the two other catalysts.

4. Conclusion

Wurtzite-type h-CoO nanoplates and nanorods have been synthesized via facile chemical solution methods. The flash-heating conditions and the presence of surfactant TOP play important roles in the formation of plate-like morphology while the choice of Co stearate as a precursor can generate nanocrystals with a rod shape. Interestingly, the UV-vis absorption spectra and the corresponding energy gaps of charge-transfer and d-d transition have been found to vary with the crystal shapes and dimensions, which emphasizes the different properties along and parallel to the (001) direction of the wurtzite-type structure. Finally all three as-prepared h-CoO nanocrystals exhibit very high catalytic activity for the hydrolysis reaction of alkaline NaBH₄ solutions. In particular, the maximum H₂ generation rate of h-CoO nanoplates is as high as 6250 ml min⁻¹ g⁻¹ at 303 K. This remarkable value exceeds most of the reported values of transition metal or noble metal containing catalysts performed in the same reaction system. The Arrhenius activation energies of h-CoO nanoplates, short nanorods and long nanorods are determined to be about 55.3, 53.0 and 42.7 kJ mol⁻¹, respectively. The obtained results demonstrate that h-CoO nanocrystals have shape-dependent optical and catalytic properties, which can

find wide applications in multiple fields. In particular, in the field of green energy, they can be a low-cost alternative to be applied in H₂ generation from the hydrolysis of various borohydrides.

Acknowledgments

The authors gratefully acknowledge financial support from the National Basic Research Program of China (No. 2012CB933103), the National Outstanding Youth Science Foundation of China (Grant No. 50825101), and the National Natural Science Foundation of China (Grant Nos 51171157 and 51171158).

References

- [1] Smith G B, Ignatiev A and Zajac G 1980 Solar selective black cobalt: preparation, structure, and thermal stability *J. Appl. Phys.* **37** 4186–96
- [2] Wang G, Shen X, Horvat J, Wang B, Liu H, Wexler D and Yao J 2009 Hydrothermal synthesis and optical, magnetic, and supercapacitance properties of nanoporous cobalt oxide nanorods *J. Phys. Chem. C* **113** 4357–61
- [3] Nam K M, Shim J H, Han D W, Kwon H S, Kang Y M, Li Y, Song H, Seo W S and Park J T 2010 Syntheses and characterization of wurtzite CoO, rocksalt CoO, and spinel Co₃O₄ nanocrystals: their interconversion and tuning of phase and morphology *Chem. Mater.* **22** 4446–54
- [4] Yamada Y, Yano K, Xu Q and Fukuzumi S 2010 Cu/Co₃O₄ nanoparticles as catalysts for hydrogen evolution from ammonia borane by hydrolysis *J. Phys. Chem. C* **114** 16456–62
- [5] Lu A, Chen Y, Jin J, Yue G H and Peng D-L 2012 CoO nanocrystals as a highly active catalyst for the generation of hydrogen from hydrolysis of sodium borohydride *J. Power Sources* **220** 391–8
- [6] Teng Y, Sakurai H, Ueda A and Kobayashi T 1999 Oxidative removal of CO contained in hydrogen by using metal oxide catalysts *Int. J. Hydrog. Energy* **24** 355–8
- [7] Li W Y, Xu L-N and Chen J 2005 Co₃O₄ nanomaterials in lithium-ion batteries and gas sensors *Adv. Funct. Mater.* **15** 851–7
- [8] Nam H J, Sasaki T and Koshizaki N 2006 Optical Co gas sensor using a cobalt oxide thin film prepared by pulsed laser deposition under various argon pressures *J. Phys. Chem. B* **110** 23081–4
- [9] Shima H, Takano F, Muramatsu H, Akinaga H, Tamai Y, Inque I H and Takagi H 2008 Voltage polarity dependent low-power and high-speed resistance switching in CoO resistance random access memory with Ta electrode *Appl. Phys. Lett.* **93** 113504
- [10] Nagashima K, Yanagida T, Oka K, Taniguchi M, Kawai T, Kim J S and Park B H 2010 Resistive switching multistate nonvolatile memory effects in a single cobalt oxide nanowire *Nano Lett.* **10** 1359–63
- [11] Seo W S, Shim J H, Oh S J, Lee E K, Hur N H and Park J T 2005 Phase- and size-controlled synthesis of hexagonal and cubic CoO nanocrystals *J. Am. Chem. Soc.* **127** 6188–9
- [12] Redman M J and Steward E G 1962 Cobaltous oxide with the zinc blende/wurtzite-type crystal structure *Nature* **193** 867
- [13] White M A, Ochsenbein S T and Gamelin D R 2008 Colloidal nanocrystals of wurtzite Zn_{1-x}Co_xO (0 ≤ x ≤ 1): models of spinodal decomposition in an oxide diluted magnetic semiconductor *Chem. Mater.* **20** 7107–16
- [14] Meyer W, Hock D, Biedermann K, Gubo M, Müller S, Hammer L and Heinz K 2008 Coexistence of rocksalt and

- wurtzite structure in nanosized CoO films *Phys. Rev. Lett.* **101** 016103
- [15] An K, Lee N, Park J, Kim S C, Hwang Y, Park J G, Kim J Y, Park J H, Han M J, Yu J and Hyeon T 2006 Synthesis, characterization, and self-assembly of pencil-shaped CoO nanorods *J. Am. Chem. Soc.* **128** 9753–60
- [16] He X and Shi H 2011 Synthesis and anomalous magnetic properties of hexagonal CoO nanoparticles *Mater. Res. Bull.* **46** 1692–7
- [17] Risbud A S, Snedeker L P, Elcombe M M, Cheetham A K and Seshadri R 2005 Wurtzite CoO *Chem. Mater.* **17** 834–8
- [18] Liu J F, He Y, Chen W, Zhang G Q, Zeng Y W, Kikegawa T and Jiang J Z 2007 Bulk modulus and structural phase transitions of wurtzite CoO nanocrystals *J. Phys. Chem. C* **111** 2–5
- [19] Liu J F, Yin S, Wu H P, Zeng Y W, Hu X R, Wang Y W, Lv G L and Jiang J Z 2006 Wurtzite-to-rocksalt structural transformation in nanocrystalline CoO *J. Phys. Chem. B* **110** 21588–92
- [20] Nam K M, Choi Y C, Jung S C, Kim Y-I, Jo M R, Park S H, Kang Y-M, Han Y K and Park J T 2012 [100] Directed Cu-doped h-CoO nanorods: elucidation of the growth mechanism and application to lithium-ion batteries *Nanoscale* **4** 473–7
- [21] Pick S 2007 Density-functional study of the CO adsorption on ferromagnetic Co(0001) and Co(111) surfaces *Surf. Sci.* **601** 5571–5
- [22] Rosca V, Beltramo G L and Koper M T M 2005 Reduction of NO adlayers on Pt(110) and Pt(111) in acidic media: evidence for adsorption site-specific reduction *Langmuir* **21** 1448–56
- [23] Jin J M, Lin W F and Christensen P A 2008 The effects of the specific adsorption of anion on the reactivity of the Ru (0001) surface towards CO adsorption and oxidation: *in situ* FTIRS studies *Phys. Chem. Chem. Phys.* **10** 3774–83
- [24] Bratlie K M, Lee H, Komvopoulos K, Yang P and Somorjai G A 2007 Platinum nanoparticle shape effects on benzene hydrogenation selectivity *Nano Lett.* **7** 3097–101
- [25] Han X, Kuang Q, Jin M, Xie Z and Zheng L 2009 Synthesis of titania nanosheets with a high percentage of exposed (001) facets and related photocatalytic properties *J. Am. Chem. Soc.* **131** 3152–3
- [26] Han X-G, He H-Z, Kuang Q, Zhou X, Zhang X-H, Xu T, Xie Z-X and Zheng L-S 2009 Controlling morphologies and tuning the related properties of nano/microstructured ZnO crystallites *J. Phys. Chem. C* **113** 584–9
- [27] Murray C B, Sun S, Doyle H and Betley T 2001 Monodisperse 3d transition-metal (Co, Ni, Fe) nanoparticles and their assembly into nanoparticle superlattices *MRS Bull.* **26** 985–91
- [28] She H, Chen Y, Chen X, Zhang K, Wang Z and Peng D-L 2012 Structure, optical and magnetic properties of Ni@Au and Au@Ni nanoparticles synthesized via non-aqueous approaches *J. Mater. Chem.* **22** 2757–65
- [29] Park J, Koo B, Yoon K Y, Hwang Y, Kang M, Park J-G and Hyeon T 2005 Generalized synthesis of metal phosphide nanorods via thermal decomposition of continuously delivered metal–phosphine complexes using a syringe pump *J. Am. Chem. Soc.* **127** 8433–40
- [30] She H, Chen Y, Wen R, Zhang K, Yue G-H and Peng D-L 2010 A nonaqueous approach to the preparation of iron phosphide nanowires *Nanoscale Res. Lett.* **5** 786–90
- [31] Hu J Q, Li Q, Wong N B, Lee C S and Lee S T 2002 Synthesis of uniform hexagonal prismatic ZnO whiskers *Chem. Mater.* **14** 1216–9
- [32] Brundle C R, Chung T J and Rice D W 1976 X-ray photoemission study of the interaction of oxygen and air with clean cobalt surfaces *Surf. Sci.* **60** 286–300
- [33] Zhang H T and Chen X H 2005 Controlled synthesis and anomalous magnetic properties of relatively monodisperse CoO nanocrystals *Nanotechnology* **16** 2288–94
- [34] He T, Chen D, Jiao X, Wang Y and Duan Y 2005 Solubility-controlled synthesis of high-quality Co₃O₄ nanocrystals *Chem. Mater.* **17** 4023–30
- [35] Kim K S 1975 X-ray-photoelectron spectroscopic studies of the electronic structure of CoO *Phys. Rev. B* **11** 2177–85
- [36] Weakliem H A 1962 Optical spectra of Ni²⁺, Co²⁺, and Cu²⁺ in tetrahedral sites in crystals *J. Chem. Phys.* **36** 2117–40
- [37] Koidl P 1977 Optical absorption of Co²⁺ in ZnO *Phys. Rev. B* **15** 2493–9
- [38] Figgis B N and Hitchman M A 2000 *Ligand Field Theory and its Application* (New York: Wiley–VCH)
- [39] Qiu X, Li G, Sun X, Li L and Fu X 2008 Doping effects of Co²⁺ ions on ZnO nanorods and their photocatalytic properties *Nanotechnology* **19** 215703
- [40] Han M J and Yu J 2006 Electronic structure and magnetic properties of wurtzite CoO *J. Korean Phys. Soc.* **48** 1496–500
- [41] Smith A M and Nie S 2010 Semiconductor nanocrystals: structure, properties, and band gap engineering *Acc. Chem. Res.* **43** 190–200
- [42] Hirschman K D, Tsybeskov L, Duttagupta S P and Fauchet P M 1996 Silicon-based visible light-emitting devices integrated into microelectronic circuits *Nature* **384** 338–41
- [43] Tong J F, Hsiao H L and Hwang H L 1999 Adjustable emissions from silicon-rich oxide films prepared by plasma-enhanced chemical-vapor deposition *Appl. Phys. Lett.* **74** 2316–8
- [44] Schlesinger H I, Brown H C, Finholt A E, Gilbreath J R, Hoekstra H R and Hyde E K 1953 Sodium borohydride, its hydrolysis and its use as a reducing agent and in the generation of hydrogen *J. Am. Chem. Soc.* **75** 215–9